energies

MDPI

Article

Design and Optimization of a Novel Wound Field Synchronous Machine for Torque Performance Enhancement

Wenping Chai [1], Thomas A. Lipo [2] and Byung-il Kwon [1,*]

[1] Department of Electronic Systems Engineering, Hanyang University, Ansan 15588, Korea; chaicool@163.com
[2] Department of Electrical and Computer Engineering, University of Wisconsin-Madison, Madison, WI 53706, USA; lipo@engr.wisc.edu
* Correspondence: bikwon@hanyang.ac.kr; Tel.: +82-31-400-5165

Received: 10 July 2018; Accepted: 13 August 2018; Published: 14 August 2018

Abstract: This paper presents the design and optimization of a novel wound field synchronous machine topology, in which permanent magnets (PMs) are introduced into the rotor slot opening with segment configuration for high quality output torque performance. The rotor shape of the proposed PM-assisted wound field synchronous machine with segment configuration is optimized for maximizing the average output torque and decreasing torque ripple under constant PM volume and motor size. The segment configuration can be benefit to improve the reluctance torque. In addition, it is further clarified that the assisted-PM can help to increase the field torque by enlarging the magnetizing synchronous reactance (X_f), as well as increasing airgap flux density. An optimal method combining Kriging method and genetic algorithm is applied for rotor shape optimization of proposed PM-assisted wound field synchronous machine (PMa-WFSM). Then, the 2-D finite-element analysis results, with the aid of JMAG-Designer, are used to confirm the validity. It is determined that the average output torque is improved by 31.66%, and keeps lower torque ripple without decreasing efficiency, increasing PM volume and motor size compared with those of the basic model. Finally, irreversible demagnetization and mises stress analysis verifies the reliability of the novel topology.

Keywords: wound field synchronous machine; PM-assisted; finite-element analysis; segment configuration; genetic algorithm; torque performance

1. Introduction

Recently, development of the industry and the environmental issue are attracting more and more attention [1,2]. Therefore, a series of new techniques about motor system topologies have been developed and applied to obtain high torque density and energy efficiency in most of the industry application and daily life [3,4].

Wound-field synchronous machines (WFSMs) utilize rotor windings to generate flux without the use of magnets. They provide some potential significant benefits and advantages including reducing material cost, higher machine system efficiencies though power factor improvements, loss minimization field control, and improved safety through direct field control during inverter fault conditions [5]. In addition, the effectiveness of WFSMs compared with a Prius Interior Permanent Magnet Motor was analyzed in [6]. It shows WFSMs have two major advantages: one is the controllable field which will make the driver more flexible, and the other one is there are no rare earth magnets. However, the current in the field winding causes significant copper loss, thereby the efficiency is decreased and temperature rise is increased. Additional brushed or brushless methods of transferring power to the rotor field winding are needed which introduces more complexity into the motor's structure.

With the development of permanent magnets (PM) such as Nd-Fe-B, permanent magnet synchronous machines (PMSMs) have been widely used in many industry applications instead of WFSMs because they are very efficient and torque-dense, as well as the size and shape of motor are flexible and varied to meet the corresponding working conditions. However, there are also some problems with PMSMs. The high cost of permanent magnet materials and the limited supply have been signed as its disadvantages [7]. The other problem is that once the magnet is magnetized, it is difficult to achieve flux weakening control [8]. Furthermore, the danger of the irreversible demagnetization should be considered when designing PMSMs.

To overcome these problems, many types of hybrid excited machines have been developed [9], and the PM-assisted wound field synchronous machine (PMa-WFSM) is one of them. In [10], a WFSM was designed for small electric-vehicle traction by inserting the permanent magnets into a predetermined position. Through the comparison of four positions and two kinds of permanent magnet materials, the combination of assisted-PM in slot opening and Nd-Fe-B is the best choice. As mentioned, all the torque ripple values of the PM-assisted models are higher than that of original model. The estimation of assist effects by additional permanent magnets has been done in [11], and these effects vary with load condition. The PM is installed in the pole head to help ensure smooth startup of the machine and improve torque density without any external aid [12]. The paper [13] investigated the mechanism of voltage increased by additional PMs with using a nonlinear magnetic circuit. This expression is useful for the designs of PMa-WFSM. The Rosenbrock's method and time-stepping adaptive FEA are chosen for optimizing the rotor shape of a PMa-WFSM for output maximization [14], while the torque ripple is not considered and the reluctance torque is still negligible.

In reference [15], the single flux barrier is introduced in WFSMs. It is a simple method to improve the motor reluctance torque and widen the operating region. Actually, the single flux barrier can bring about an imbalance of magnetic flux density of the two steel pieces in each pole. Thus, the position of the single flux barrier is considered to be one of the optimal variables [16] to get higher saliency ratio. Nevertheless, the torque ripple is still unsatisfactory because of the asymmetrical single flux barrier.

In this study, PM was introduced into the rotor slot opening of a WFSM with segment configuration for high-quality output torque performance. The rotor shape of proposed PMa-WFSM was optimized for improving the average output torque and keeping lower torque ripple under constant PM volume and motor size. The optimization method mainly comprises Kriging method and a genetic algorithm (GA). Then, JMAG-Designer has been used as the tool of finite-element analysis (FEA) to confirm the validity. Finally, the magnetic saturation under the condition of no-load affected by assisted-PM and its irreversible demagnetization effect and mises stress analysis were analyzed.

2. Analysis of the Investigated Motor

2.1. The Basic WFSM

To highlight the advantages of the proposed approaches, a WFSM with conventional pole head and segment configuration designated is adopted as the basic model. The stator has six slots with three-phase concentrated coil windings as shown in Figure 1a. The basic rotor of WFSM is shown in Figure 1b. All the specifications of the basic model are listed in Table 1.

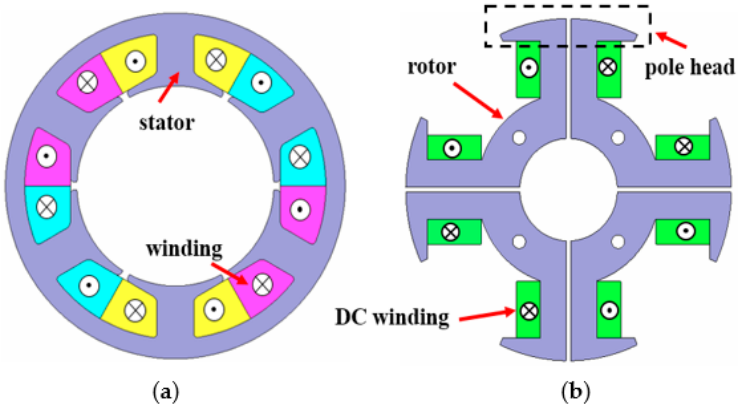

Figure 1. Topology of the basic model. (**a**) Stator (**b**) Basic rotor.

Table 1. Specifications of the basic model.

Item	Unit	Basic
Slots/poles	-	6/4
Rated current	A	1.6
Rated speed	rpm	1500
Stator outer diameter	mm	88
Stator inter diameter	mm	51
Airgap length	mm	0.5
Motor axial length	mm	52
Magnetic motive force	At	80
Segment distance	mm	0.7
Magnet volume	mm^3	0
Rotor slot filling ratio	-	0.45–0.60

2.2. The Proposed Model with Assisted-PM

The topology of the proposed model is presented in Figure 2. The PM is assisted in the rotor slot opening and a small protruding piece of steel on the teeth is used for fixing the PM. In this section, NEOMAX-50 (Hitachi, Tokyo, Japan) is selected as the assisted-PM for the hybrid excitation and the PM volume is 4 × 3 mm × 12 mm × 52 mm. It shares the same stator with the basic model. However, the PM needs to be fixed in the opening of the rotor slot, the pole head shape should be changed for adaption. Theoretically, the ratio of pole arc to pole pitch has a range of 0.65 to 0.75 [17]. This will make that the design of field system becomes economical. Therefore, it is necessary to analyze the optimum structure in the following section.

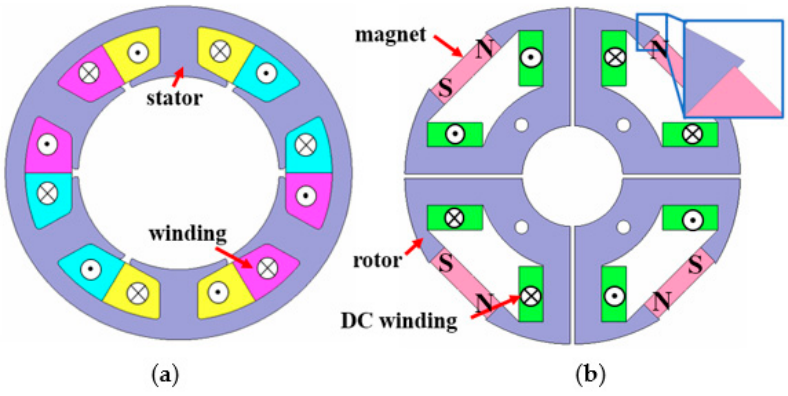

Figure 2. Topology of the proposed model: (**a**) Stator; (**b**) Proposed rotor.

2.3. Electromagnetic Performance Analysis

2.3.1. Principle

In fact, because of the adaptive pole head shape due to the assisted-PM, the length of q-axis flux path in the steel core will be increased. This will make the saliency reduced. It is not good for the high torque density. Therefore, the segment configuration and pole head should be paid more attention.

The Figure 3a shows the phasor diagram of proposed model derived from d-q rotor frame equivalent circuit using the Park transformation, where winding resistances and space harmonics are neglected. The terminal voltage in the circuit can be expressed as follows:

$$\begin{aligned} U_d &= I_q X_q \\ U_q &= -I_d X_d + X_f I_f + w_0 \psi_{PM} \end{aligned} \tag{1}$$

where, U_d and U_q are the d-axis and the q-axis terminal voltages, I_d and I_q are the d-axis and the q-axis magnetizing currents, X_d and X_q are the d-axis and the q-axis synchronous reactance, X_f is the magnetizing synchronous reactance, I_f is the DC field current, ψ_{PM} is the maximum flux linkages by the PM, w_0 is the electrical frequency. The electromagnetic torque can be calculated from the circuit as expressed in Equation (2).

$$\begin{aligned} T &= \frac{P}{n} = \frac{U_d I_d + U_q I_q}{n} \\ &= \frac{1}{n}\left[I_s I_f X_f \cos\gamma + I_s w_0 \psi_{PM} \cos\gamma - 0.5(X_d - X_q) I_s^2 \sin 2\gamma \right] \end{aligned} \tag{2}$$

where, I_s is the peak value of the phase current, γ is the angle of the stator current vector measured with respect to the q-axis designated as the current phase angle. The first term is the field torque, the second is the PM torque, and the last is the reluctance torque. Theoretically, the three torques are both benefit for the total torque of the motor. The high X_f, ψ_{PM} and $X_d - X_q$ will increase the total torque.

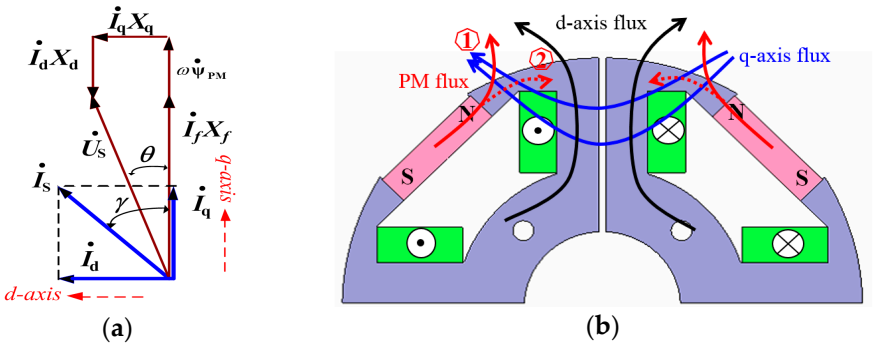

Figure 3. (**a**) Vector diagram in d-q reference frame; (**b**) Magnetic flux path on the rotor.

Figure 3b shows the magnetic flux path on the rotor of proposed PMa-WFSM. The PM flux is separated by part 1 and part 2 in the assisted position. The PM flux part 1 not only increases the air gap flux density directly, but also can decrease the q-axis flux path in the pole head that can reduce the inductance of q-axis, which has the same function of the segment configuration. The PM flux part 2 in Figure 3b can be seen that it can mitigate the flux in the iron core and the X_f will be increased because of low magnetic saturation.

The segment rotor pole can decrease the X_q which can be benefit for the saliency. The d-axis and q-axis flux distribution are shown in Figure 4. Assume that the position where the rotor pole is opposed to the stator teeth is the d-axis. In addition, turning counterclockwise 90-degree electrical angle along the d-axis is the q-axis. The q-axis flux line closed to the segmental edges form a zigzag

leakage path, which shows the flux lines find a low reluctance path to be a circle. In addition, from the view of the rotor pole head, the q-axis flux line is also limited by the PM flux.

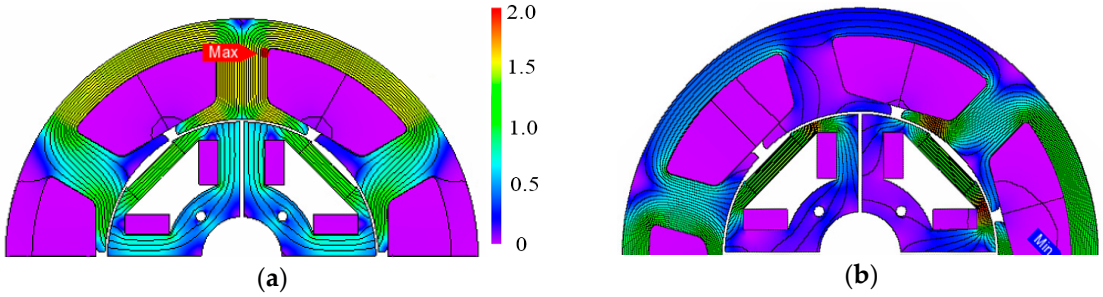

Figure 4. Flux distribution for proposed structure. (**a**) d-axis; (**b**) q-axis.

To verify the above analysis, the 2-D FEA (JMAG-Designer) is used. Figure 5a shows the total magnetic flux distributions of proposed model under no-load condition. In addition, the frozen permeability method (FPM) [18] is used to obtain the separated magnetic flux produced by the rotor field windings (FWs) or produced by the assisted-PM, as indicated in Figure 5b,c. It is observed that the magnetic flux direction of the PM in the rotor core is opposite to that produced by the FWs. It can reduce the magnetic saturation of the pole core, which further influence X_f. It is benefit for the enhancement of the field torque. Some of magnetic flux produced by the assisted-PMs flow through the air gap into the stator core. Its direction is the same as that of the flux flows produced by the FWs. The magnetic flux of this part will increase the airgap flux density. It is benefit for improving electromagnetic torque.

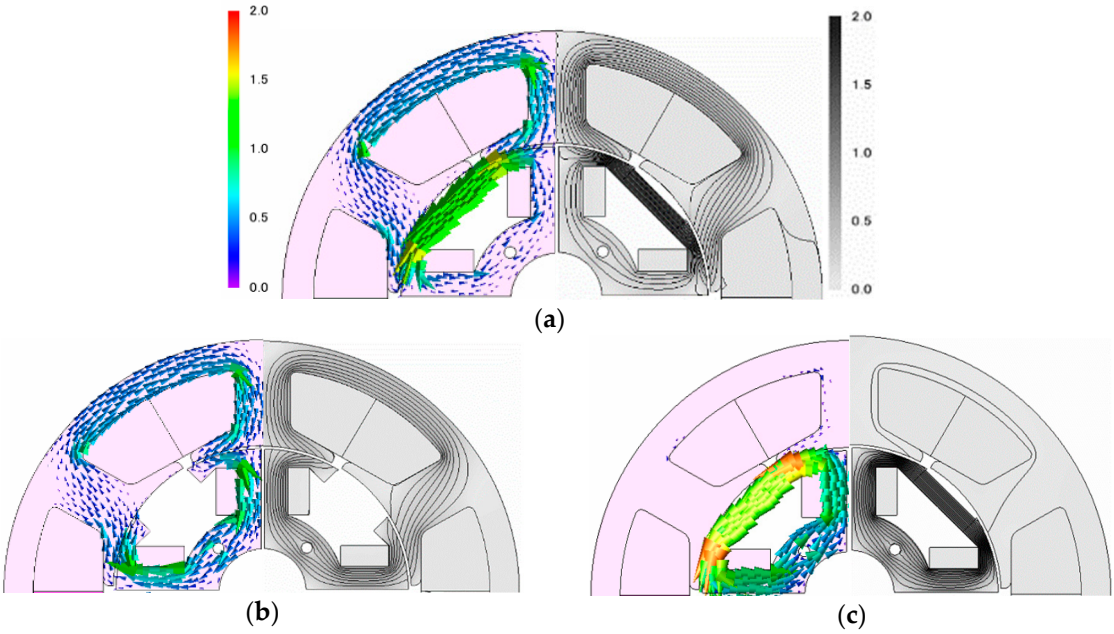

Figure 5. Total and separated magnetic flux. (**a**) Total magnetic flux; (**b**) Magnetic flux produced by FWs; (**c**) Magnetic flux produced by assisted-permanent magnets (assisted-PMs).

2.3.2. The Performance Comparison between the Basic and Proposed Models

Figure 6 shows the torque characteristics of basic model and proposed model, respectively. At the current phase angle of $-25°$, the output torque can reach their maximum values. Compared with the basic model, additional magnet torque is added and contributes 9.9% of the total torque, meanwhile

the average output torque is increased by 17.55%. Meanwhile, the reluctance torque is increased by only 6.9%. It is enough to verify that the assisted-PM flux can effectively decrease the X_q reduction, which is caused by the change of the pole head shape for installing PM. However, as is known in the published papers [10–16], the torque ripple has the challenge of deterioration. As far as this motor is concerned, the torque ripple is increased by 44.5%, it can be shown in Figure 7 and Table 2. Figure 8 shows the calculated no-load saturation curves of the basic model and proposed model. It is revealed that the saturation field current of the basic and proposed model is changed from 1.7 A to 2.6 A. It is observed that it benefits from reduction in the magnetic saturation of the core by assisted-PM. In the following section, the segment distance and segment displacement, the shape of magnet and pole head will be optimized to realize higher average torque and lower torque ripple.

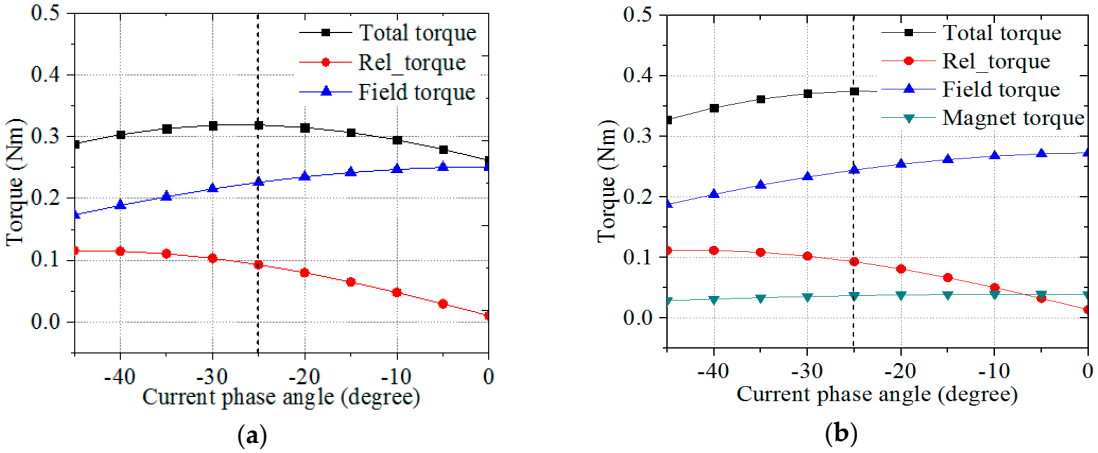

Figure 6. The torque characteristics: (**a**) Basic model; (**b**) Proposed model.

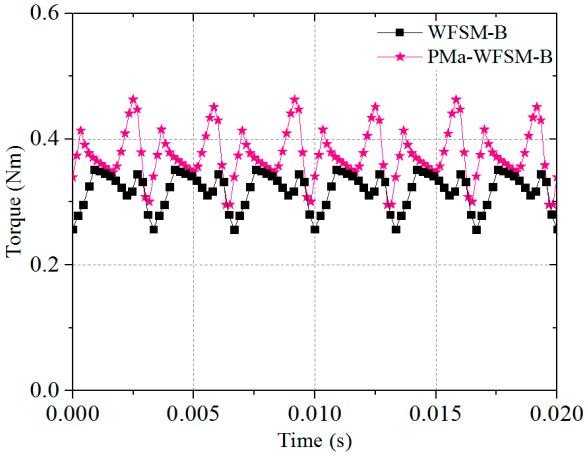

Figure 7. The electromagnetic torques.

Table 2. Analysis results of basic model and proposed model.

Item	Unit	Basic	Proposed
Power@1500	W	50.11	58.90
Torque	Nm	0.319	0.375
Reluctance torque	Nm	0.087	0.093
Efficiency	%	87.6	87.5
Torque ripple	%	29.9	44.7

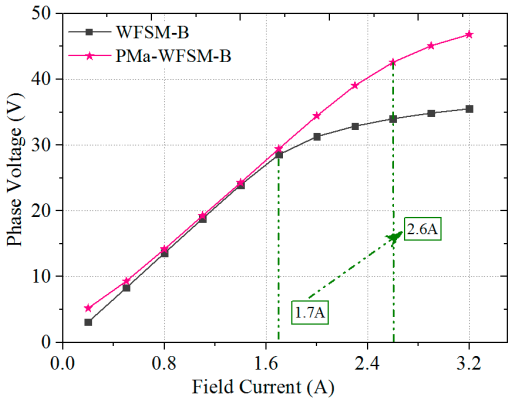

Figure 8. Calculated saturation curves.

3. Rotor Shape Optimization

3.1. The Process of Rotor Shape Optimization

The abovementioned proposed PMa-WFSM was designed only by adding PMs in the slot opening of the WFSM segmented rotor. It not only brings the increase of the average output torque but also causes the deterioration of the torque ripple. This characteristic is more obvious in the segment configuration. It is expected that the average output torque and torque ripple can be improved by optimizing the shape of the proposed rotor. Therefore, an effective optimization approach combining Kriging method [19] and genetic algorithm (GA) [20] is applied for rotor shape optimization in order to improve torque characteristic and decrease torque ripple under constant PM volume and motor size without the deterioration of efficiency.

Figure 9 shows the five design variables assigned to the rotor. The width h of the assisted-PM is selected as one of the design variables, whereas the length w of the assisted-PM is automatically changed in order to maintain the volume of assisted-PM as a constant. m and l are the main parameters that define the rotor slot area and the magnetic flux path of the assisted-PM. d is the segment distance that can determine the ability of hindering the q-axis flux. x is the segment displacement between the rotor pole center and segment distance center which can adjust the magnetic imbalance of the two pieces in each rotor pole. Because the assisted-PM changes the across-sectional area of the FWs, in order to maintain the slot filling ratio, the number of turns is proportionately changed. The stator is fixed during the entire optimization process of the motor.

Firstly, according to the requirements of the motor, the objective functions, constraints, and design variables are obtained. The main optimal design process can be classified as roughly two steps as shown in Figure 10.

(1) The Latin Hypercube Sampling (LHS) [21] step of process 1 in Figure 10 is the first step of searching the optimized design variables in the design range of design variables h, m, l, d, and x. By using the LHS within the design range corresponding to the determined design variables, the sampling values are randomly and evenly distributed in all areas. The model approximated by the 2D FEA analysis results is composed by using the Krigging method in the PIAnO software (v.3.6, PIDOTEC Inc, Seoul, South Korea) by PIDOTEC Inc. [22].

(2) For this paper, the Generic Algorithm step of process 2 in Figure 10 evaluates the fitness from the modeling function developed by the Kriging model; thus, the optimal results were determined by the population. The fitness modeling function $F(i)$ used in GA is expressed as [23]

$$F(i) = f(i) + \varepsilon P(i) \tag{3}$$

where $f(i)$ is the multi-objective function, $P(i)$ is the penalty function, ε is the penalty coefficient, and i is vector of the design variables.

Finally, the optimal design results were verified by FEA. If the FEA results were not satisfied with the target requirements, the range of design variables should be adjusted and do the above steps again, until it is satisfied.

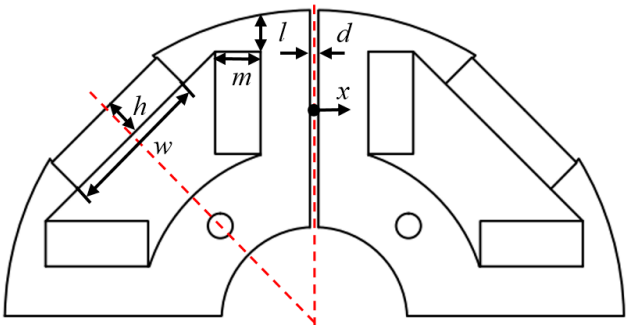

Figure 9. Design variables.

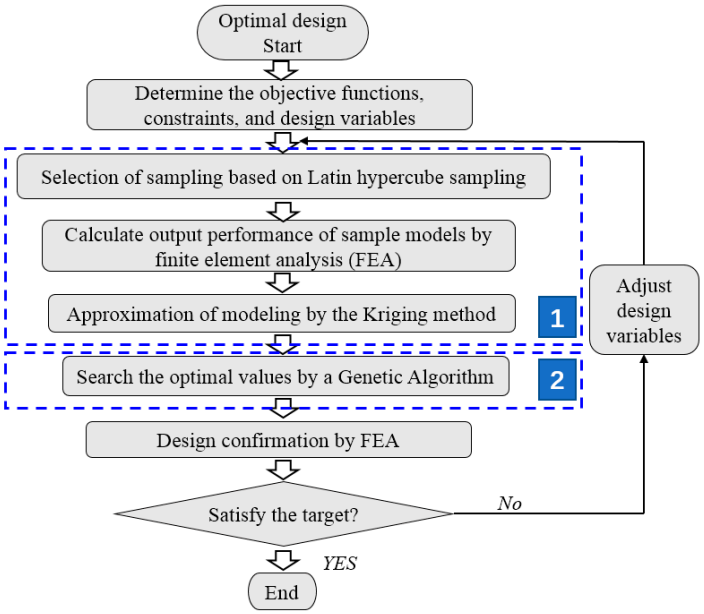

Figure 10. Optimal design process.

The objective functions for maximizing the total torque and minimizing the torque ripple are shown in Equation (4), which are implemented with the same weight value to each objective function. Compared with proposed model, the constraints are set to limit the total torque to a higher value, and the torque ripple should be lower, as shown in Equation (5). It is simple and easy implementation to be conducted through the commercial optimization tool–PIAnO. The ranges for the design variables are shown in Equation (6).

- Objective functions:

$$\begin{array}{l} \text{Maximize the total torque.} \\ \text{Minimize the torque ripple.} \end{array} \quad (4)$$

- Constraints:

$$\begin{array}{l} \text{Torque} > 0.37\ \text{Nm} \\ \text{Torque ripple} < 44.7\% \end{array} \quad (5)$$

- Design variables:

$$\begin{aligned} 0.7\text{ mm} &\leq d \leq 1.1\text{ mm} \\ 0\text{ mm} &\leq x \leq 1\text{ mm} \\ 3\text{ mm} &\leq l \leq 6\text{ mm} \\ 0\text{ mm} &\leq m \leq 4\text{ mm} \\ 3\text{ mm} &\leq h \leq 6.1\text{ mm} \end{aligned} \tag{6}$$

3.2. Optimal Design Results and Discussion

3.2.1. Convergence Results of Variables

In the optimization process, the optimal values of the variables for the objective functions can be obtained. The convergence results of the design variables are shown in Figure 11a. The five design variables (h, l, m, d, x) are 5.612 mm, 3.662 mm, 2.289 mm, 1.075 mm, 0.003 mm, respectively. When the average torque and torque ripple are kept the same weight value, the segment displacement x is closed to 0, which indicates that the segment displacement x is the contradictory between the average torque and torque ripple. Figure 11b shows the convergence procedure and results of the optimized design of torque and torque ripple of the objective function. The determined average output torque and torque ripple after the iteration are 0.425 Nm and 27.72%, respectively.

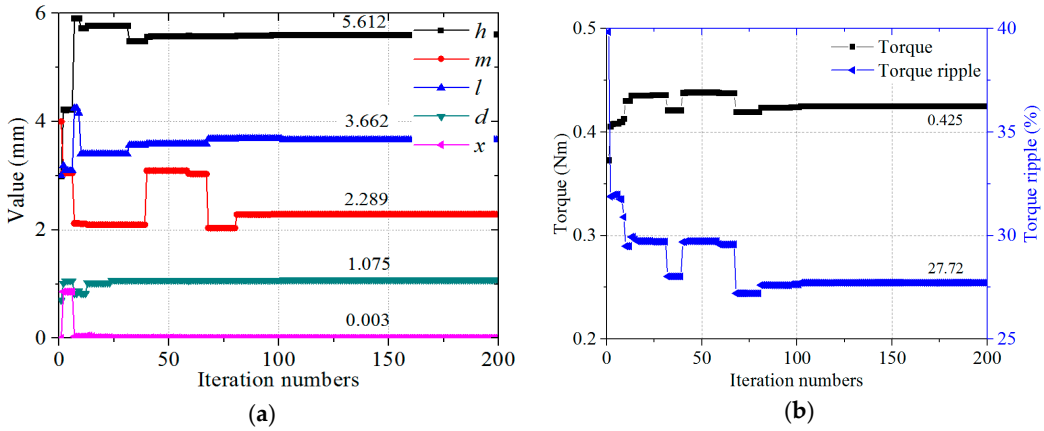

Figure 11. Convergence process: (**a**) design variables; (**b**) objective function.

3.2.2. Characteristics Analysis Results by 2-D FEA

The design variables obtained by iteration have been used to verify in JMAG-2D designer as the optimal model. Figure 12 shows the torque characteristics of the optimal model, and the detail analysis results from simulation is revealed in Table 3. At the current phase angle of $-25°$ that is the same with basic model and proposed model, the output torque can reach its maximum value. The assisted-PM in the optimal model is better utilized than that in proposed model. Compared with the proposed model results, the total torque is increased by 12%, apparently. The sum of the reluctance torque and the magnet torque increases from 23.4% of the total torque to 38.3%.

The electromagnetic torques of proposed model and optimal model at the maximum torque condition are compared in Figure 13. The torque ripple of the optimal model, defined as the peak to peak torque value versus the average torque value is reduced by 35.1% compared to that of the proposed model.

The electromotive force is produced by the field current and the assisted-PM. Figure 14 shows the calculated no-load saturation curves of the proposed model and optimal model. It is revealed that the phase voltage of proposed model and optimal model has an increase of around 1.8 V. This is mainly caused by the direct flux linkage of the armature winding from the assisted-PM.

Table 3. Analysis results of optimal model.

Item	Unit	Optimal
Power@1500	W	65.97
Torque	Nm	0.420
Reluctance torque	Nm	0.095
Efficiency	%	87.6
Torque ripple	%	29.0

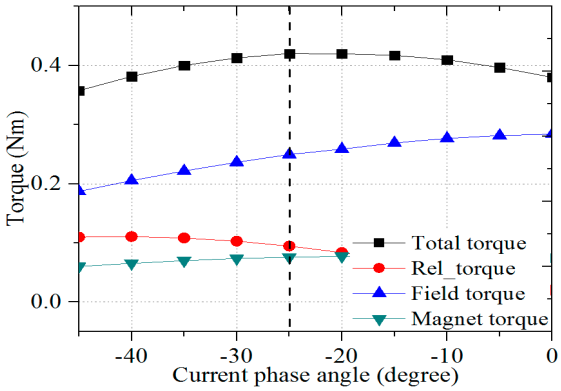

Figure 12. The torque characteristics of optimal model.

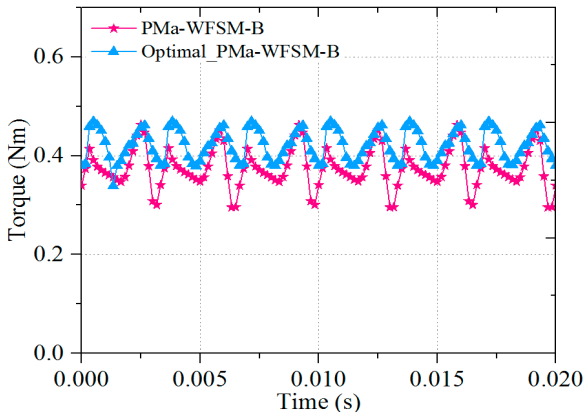

Figure 13. The electromagnetic torques of proposed and optimal model.

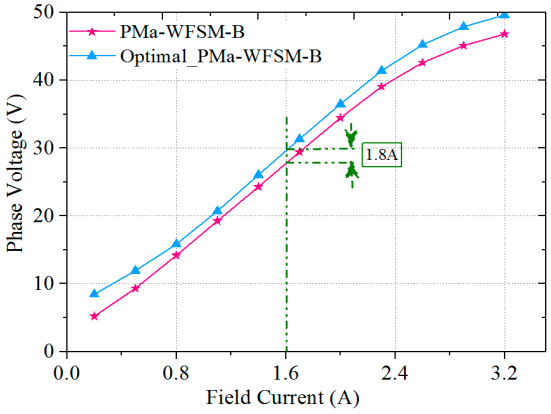

Figure 14. Calculated saturation curve of proposed model and optimal model.

4. Performance Comparison

4.1. Back Electromotive Forces (Back-EMFs)

Figure 15 shows the comparison of Back-EMFs for each phase. Due to the optimization of the pole head, the Back-EMF of the optimal model exhibit considerable distortion but contain highly enhanced fundamental value. Figure 16 shows the corresponding Fast Fourier Transform (FFT) analysis, while the Total Harmonics Distortion (THD) for the three models are 6.5%, 3.13% and 1.51%, respectively.

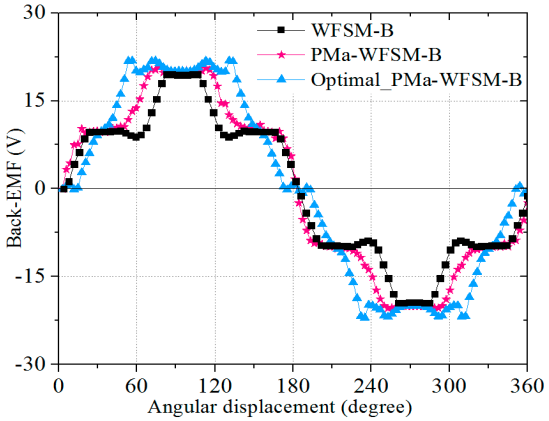

Figure 15. Comparison of Back Electromotive Forces (Back-EMFs) in phase.

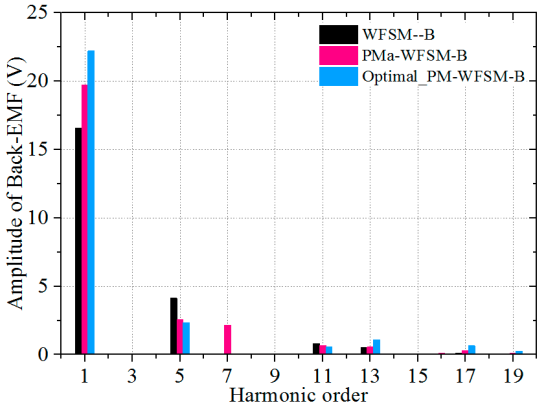

Figure 16. Harmonic analysis of back-EMFs.

4.2. The Magnetic Flux Density Distribution

The magnetic flux density distribution of basic model, proposed model and optimal model at the maximum torque condition are shown in Figure 17a–c, respectively. It is shown that the magnet flux density of the rotor core has been reducing effectively and the magnetic flux density of the stator core has been increased, under on-load condition. To investigate the reality clearly, there are four working points chosen for comparison as the following results.

$$\text{basic model} \begin{cases} \text{Point1} : 0.87\text{T} \\ \text{Point2} : 1.25\text{T} \\ \text{Point3} : 0.73\text{T} \\ \text{Point4} : 0.79\text{T} \end{cases}, \text{proposed model} \begin{cases} \text{Point1} : 0.34\text{T} \\ \text{Point2} : 0.48\text{T} \\ \text{Point3} : 0.78\text{T} \\ \text{Point4} : 0.85\text{T} \end{cases}, \text{optimal model} \begin{cases} \text{Point1} : 0.31\text{T} \\ \text{Point2} : 0.36\text{T} \\ \text{Point3} : 0.81\text{T} \\ \text{Point4} : 0.89\text{T} \end{cases}$$

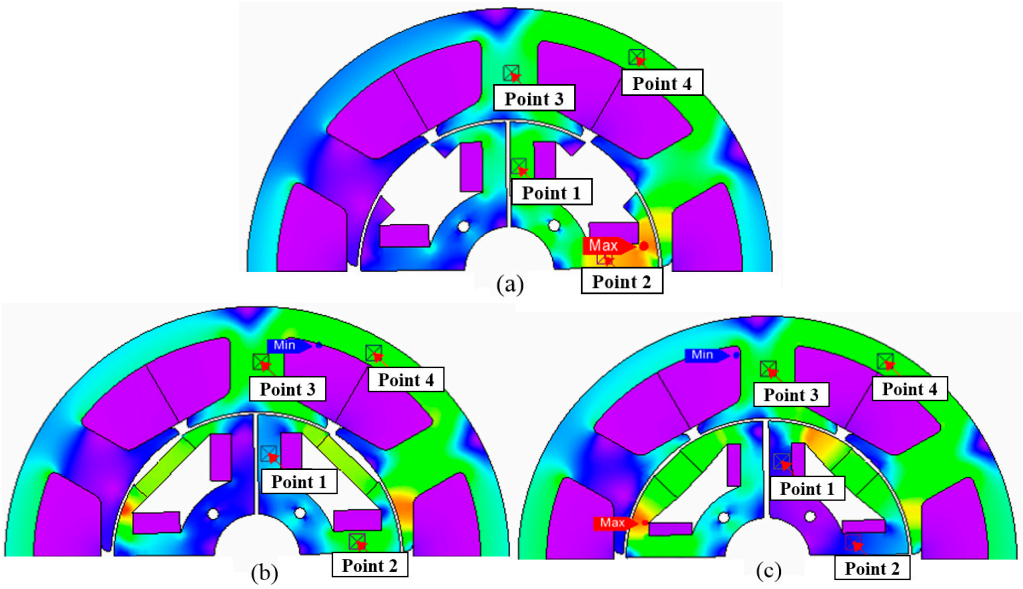

Figure 17. Magnetic flux density distribution at the maximum torque condition: (**a**) Basic model; (**b**) Proposed model; (**c**) Optimal model.

4.3. Demagnetization Analysis

When the motor suffers the sudden three phase short circuit condition, the field and armature current would be very large to keep the flux linkage as a constant. Therefore, it is necessary to analyze the irreversible demagnetization of the PM to ensure the reliability of the novel topology.

To assure the reliability of the PM utilization, the analysis of the magnet irreversible demagnetization for the optimal model is performed within seven times of the rated input current. To investigate the effect of magnet irreversible demagnetization for PM torque and field torque, the EMF demagnetization ratio is defined as

$$\delta_1 = \frac{E_1 - E_2}{E_1} \tag{7}$$

where E_1 is the Root-Mean-Square (RMS) value of the terminal voltage in phase before inputting the phase current, and E_2 is the RMS value of the terminal voltage in phase after inputting the phase current.

The analysis results of the EMF demagnetization ratios are depicted in Figure 18. It indicates that the EMF demagnetization ratio is 0.73% with seven times of the input current indicating that only a slight demagnetization occurs to the peak of the magnet.

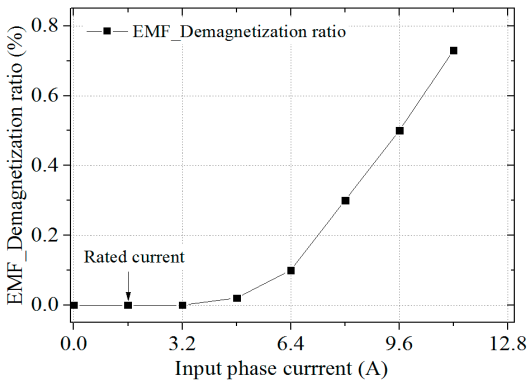

Figure 18. EMF demagnetization ratios of the optimized model.

Because the reluctance torque is affected by the assisted-PM in the optimal model, the EMF demagnetization ratio cannot describe the influence. To investigate the effect of magnet irreversible demagnetization for total torque, the torque demagnetization ratio is defined as

$$\delta_2 = \frac{T_1 - T_2}{T_1} \tag{8}$$

where T_1 is the average value of the output torque before inputting the phase current, and T_2 is the average value of the output torque after inputting the phase current.

The analysis results of the torque demagnetization ratios are depicted in Figure 19. It indicates that the torque demagnetization ratio is under 0.01% with seven times of the input current. In another word, when the motor suffers the sudden three phase short circuit condition, the demagnetization caused by the large instantaneous current will not affect the output torque of the optimal model.

From the above analysis, the demagnetization that occurs on the peak of the magnet with seven times of the input current has a negligible impact on the output performance of the optimal model. It has superior endurance against the magnet irreversible demagnetization, which especially benefits of the reluctance torque resisting the effect of demagnetization.

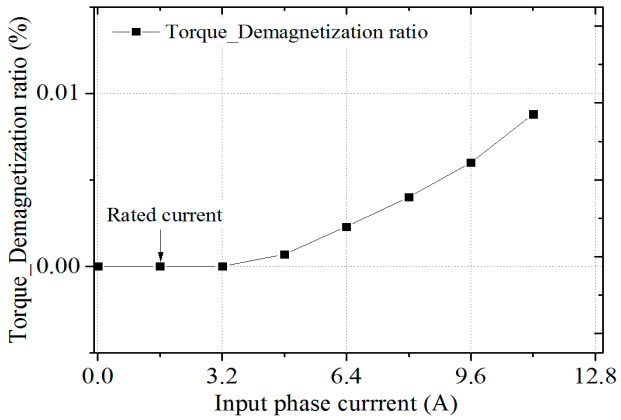

Figure 19. Torque demagnetization ratios of the optimized model.

4.4. Mises Stress Analysis

Due to the combined rotor structure, the mechanical stress of the machine at the rated speed-1500 r/min has to be investigated. The material properties of the rotor core are listed in Table 4. The structural strength of the optimal model is evaluated by using FEA simulations. The maximum allowable fatigue stress (Yield strength) of the used rotor material is 304 MPa. In addition, the mises stress analysis is shown in Figure 20. It can be seen that the highest stress is about 0.5 MPa, which is so far below the maximum allowable fatigue stress of the used rotor material.

Table 4. Material properties of rotor core.

Quantity	Unit	Value
Density	Kg/m^3	7700
Young's modulus	GPa	207
Poisson's ratio	-	0.3
Tensile strength	MPa	451
Yield strength	MPa	304

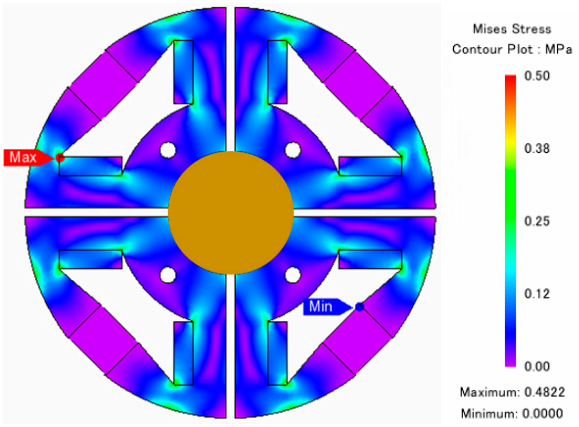

Figure 20. Mises stress distribution.

5. Conclusions

This paper proposes a novel rotor structure named proposed PMa-WFSM and then optimizes the rotor shape to improve average output torque and decrease torque ripple under a constant PM volume and motor size. It is revealed that the inflection point of iron magnetic saturation has been effectively widened, and the torque performance has been a nice enhancement. The segment distance and segment displacement, the shape of magnet and pole head should be designed and optimized for a better combination to realize the targets.

The results obtained by FEA show that the optimized model has greatly increased the total average torque by 31.66%. It is also clarified that the optimum structure can significantly reduce the torque ripple that caused by the assisted-PM. All the operations are without a decrease in efficiency or an increase on PM volume and motor size. Finally, irreversible demagnetization and mises stress analysis verified the reliability of the novel topology.

Author Contributions: T.A.L. conceived the basic idea and help English correction; W.C. designed the basic model, performed the optimization, analyzed and compared the results and wrote this paper; B.-i.K. supervised the research throughout. All the authors have contributed significantly to this work.

Funding: This work was supported in part by the Human Resources Program in Energy Technology of the Korea Institute of Energy Technology Evaluation and Planning (KETEP), granted financial resource from the Ministry of Trade, Industry & Energy, Republic of Korea (No. 20154030200730), and in part by the BK21PLUS Program through the National Research Foundation of Korea within the Ministry of Education.

Conflicts of Interest: The authors declare no conflict of interest.

References

1. Cheng, M.; Sun, L.; Buja, G.; Song, L. Advanced electrical machines and machine-based systems for electric and hybrid vehicles. *Energies* **2015**, *8*, 9541–9564. [CrossRef]
2. Cetin, E.; Daldaban, F. Analyzing distinctive rotor poles of the axial flux PM motors by using 3D-FEA in view of the magnetic equivalent circuit. *Eng. Sci. Technol. Int. J.* **2017**, *20*, 1421–1429. [CrossRef]
3. Liu, W.; Lipo, T.A. A family of vernier permanent magnet machines utilizing an alternating rotor leakage flux blocking design. In Proceedings of the 2017 IEEE Energy Conversion Congress and Exposition (ECCE), Cincinnati, OH, USA, 1–5 October 2017.
4. Yang, Y.P.; Shih, G.Y. Optimal Design of an Axial-Flux Permanent-Magnet Motor for an Electric Vehicle Based on Driving Scenarios. *Energies* **2016**, *9*, 285. [CrossRef]
5. Di Gioia, A.; Brown, I.P.; Nie, Y.; Knippel, R.; Ludois, D.C.; Dai, J.; Hagen, S.; Alteheld, C. Design and Demonstration of a Wound Field Synchronous Machine for Electric Vehicle Traction with Brushless Capacitive Field Excitation. *IEEE Trans. Ind. Appl.* **2018**, *54*, 1390–1403. [CrossRef]

6. Dorrell, D.G. Are wound-rotor synchronous motors suitable for use in high efficiency torque-dense automotive drives? In Proceedings of the IECON 2012—38th Annual Conference on IEEE Industrial Electronics Society, Montreal, QC, Canada, 25–28 October 2012.
7. Boldea, I.; Tutelea, L.N.; Parsa, L.; Dorrell, D. Automotive electric propulsion systems with reduced or no permanent magnets: An overview. *IEEE Trans. Ind. Electron.* **2014**, *61*, 5696–5711. [CrossRef]
8. Tursini, M.; Chiricozzi, E.; Petrella, R. Feedforward flux-weakening control of surface-mounted permanent-magnet synchronous motors accounting for resistive voltage drop. *IEEE Trans. Ind. Electron.* **2010**, *57*, 440–448. [CrossRef]
9. Hlioui, S.; Amara, Y.; Hoang, E.; Lecrivain, M.; Gabsi, M. Overview of hybrid excitation synchronous machines technology, In Proceedings of the 2013 International Conference on Electrical Engineering and Software Applications (ICEESA), Hammamet, Tunisia, 21–23 March 2013.
10. Hwang, S.-W.; Sim, J.-H.; Hong, J.-P.; Lee, J.; Kim, J. Torque improvement of wound field synchronous motor for electric vehicle by PM-assist. *IEEE Trans. Ind. Appl.* **2018**, *54*, 3252–3259. [CrossRef]
11. Yamazaki, K.; Nishioka, K.; Shima, K.; Fukami, T.; Shirai, K. Estimation of assist effects by additional permanent magnets in salient-pole synchronous generators. *IEEE Trans. Ind. Electron.* **2012**, *59*, 2515–2523. [CrossRef]
12. Ali, Q.; Atiq, S.; Lipo, T.A.; Kwon, B.I. PM assisted, brushless wound rotor synchronous machine. *J. Magn.* **2016**, *21*, 399–404. [CrossRef]
13. Yamazaki, K.; Tamiya, S.; Shima, K.; Fukami, T.; Shirai, K. Modeling of salient-pole synchronous machines assisted by permanent magnets. *IEEE Trans. Magn.* **2011**, *47*, 3028–3031. [CrossRef]
14. Yamazaki, K.; Tamiya, S.; Utsuno, K.; Shima, K.; Fukami, T.; Sato, M. Rotor Shape Optimization for Output Maximization of Permanent-Magnet-Assisted Synchronous Machines. *IEEE Trans. Ind. Appl.* **2015**, *51*, 3077–3085. [CrossRef]
15. Liu, W.; Lipo, T.A. On saliency enhancement of salient pole wound field synchronous machines. In Proceedings of the 2016 IEEE Energy Conversion Congress and Exposition (ECCE), Milwaukee, WI, USA, 18–22 September 2016.
16. Chai, W.; Zhao, W.; Kwon, B.-I. Optimal Design of Wound Field Synchronous Reluctance Machines to Improve Torque by Increasing the Saliency Ratio. *IEEE Trans. Magn.* **2017**, *53*, 8206604. [CrossRef]
17. Toliyat, H.A.; Kliman, G.B. *Handbook of Electric Motors*, 2nd ed.; CRC Press: Boca Raton, FL, USA, 2004.
18. Walker, J.A.; Dorrell, D.G.; Cossar, C. Flux-linkage calculation in permanent-magnet motors using the frozen permeabilities method. *IEEE Trans. Magn.* **2005**, *41*, 3946–3948. [CrossRef]
19. Nielsen, H.B.; Lophaven, S.N.; Søndergaard, J. A Matlab Kriging Toolbox. In *Informatics and Mathematical Modelling*; Technical University of Denmark (DTU): Lyngby, Denmark, 2002.
20. Han, K.J.; Cho, H.S.; Cho, D.H.; Jung, H.K. Optimal core shape design for cogging torque reduction of brushless DC motor using genetic algorithm. *IEEE Trans. Magn.* **2000**, *36*, 1927–1931.
21. Viana, F.; Venter, G.; Balabanov, V. An algorithm for fast optimal Latin hypercube design of experiments. *Int. J. Numer. Methods Eng.* **2010**, *82*, 135–156. [CrossRef]
22. PIAnO Introduction. Available online: http://pidotech.com/en/product/piano.aspx (accessed on 1 April 2018).
23. Kim, J.B.; Hwang, K.Y.; Kwon, B.I. Optimization of Two-Phase In-Wheel IPMSM for Wide Speed Range by Using the Kriging Model Based on Latin Hypercube Sampling. *IEEE Trans. Magn.* **2011**, *47*, 1078–1081. [CrossRef]